Cancer Nanotechnology

RESEARCH Open Access

Photothermal therapy of papillary thyroid cancer tumor xenografts with targeted thyroid stimulating hormone receptor antibody functionalized multiwalled carbon nanotubes

Seung Soo Lee[1,2], Fatma Oudjedi[3], Andrew G. Kirk[3], Miltiadis Paliouras[1,2,4*] and Mark A. Trifiro[1,2,5]

*Correspondence:
miltiadis.paliouras@mcgill.ca

[1] Lady Davis Institute for Medical Research, Jewish General Hospital, 3755 Cote-Ste-Catherine Rd., Montreal, QC H3T 1E2, Canada
[2] Division of Experimental Medicine, Department of Medicine, McGill University, Montreal, QC, Canada
[3] Department of Electrical and Computer Engineering, McGill University, Montreal, QC, Canada
[4] Department of Oncology, McGill University, Montreal, QC, Canada
[5] Division of Endocrinology, Jewish General Hospital, Montreal, QC, Canada

Abstract

Multiwalled carbon nanotubes (MWCNTs) are being widely investigated in multiple biomedical applications including, and not limited to, drug delivery, gene therapy, imaging, biosensing, and tissue engineering. Their large surface area and aspect ratio in addition to their unique structural, optical properties, and thermal conductivity also make them potent candidates for novel hyperthermia therapy. Here we introduce thyroid hormone stimulating receptor (TSHR) antibody–conjugate–MWCNT formulation as an enhanced tumor targeting and light-absorbing device for the photoablation of xenografted BCPAP papillary thyroid cancer tumors. To ensure successful photothermal tumor ablation, we determined three key criteria that needed to be addressed: (1) predictive pre-operational modeling; (2) real-time monitoring of the tumor ablation process; and (3) post-operational follow-up to assess the efficacy and ensure complete response with minimal side effects. A COMSOL-based model of spatial temperature distributions of MWCNTs upon selected laser irradiation of the tumor was prepared to accurately predict the internal tumor temperature. This modeling ensured that 4.5W of total laser power delivered over 2 min, would cause an increase of tumor temperature above 45 ℃, and be needed to completely ablate the tumor while minimizing the damage to neighboring tissues. Experimentally, our temperature monitoring results were in line with our predictive modeling, with effective tumor photoablation leading to a significantly reduced post 5-week tumor recurrence using the TSHR-targeted MWCNTs. Ultimately, the results from this study support a utility for photosensitive biologically modified MWCNTs as a cancer therapeutic modality. Further studies will assist with the transition of photothermal therapy from preclinical studies to clinical evaluations.

Keywords: Papillary thyroid cancer, Thyroid stimulating hormone receptor, Multiwalled carbon nanotubes, Photothermal therapy, Thermal modeling, Biodistribution, Tumor recurrence, Tumor xenograft animal mouse, Nanotherapeutics

© The Author(s) 2023. **Open Access** This article is licensed under a Creative Commons Attribution 4.0 International License, which permits use, sharing, adaptation, distribution and reproduction in any medium or format, as long as you give appropriate credit to the original author(s) and the source, provide a link to the Creative Commons licence, and indicate if changes were made. The images or other third party material in this article are included in the article's Creative Commons licence, unless indicated otherwise in a credit line to the material. If material is not included in the article's Creative Commons licence and your intended use is not permitted by statutory regulation or exceeds the permitted use, you will need to obtain permission directly from the copyright holder. To view a copy of this licence, visit http://creativecommons.org/licenses/by/4.0/. The Creative Commons Public Domain Dedication waiver (http://creativecommons.org/publicdomain/zero/1.0/) applies to the data made available in this article, unless otherwise stated in a credit line to the data.

Introduction

The global incidence of thyroid cancer has been increasing over the last few decades, with over 52,000 new cases in the United States alone in 2019 (Kim et al. 2020; French 2020; Wang and Sosa 2018). Differentiated thyroid cancer accounts for more than 95% of all thyroid cancer cases, of which papillary thyroid cancer (PTC) is the most common subtype (Cabanillas et al. 2016). Diagnostic procedures such as ultrasound and fine-needle aspiration biopsy have made early detection possible. However, clinicians are often provided with limited treatment options such as total thyroidectomy. Surgical procedures are often followed by radioactive iodine remnant ablation and accompanied by thyroid stimulating hormone (TSH)-suppressive therapies using levothyroxine or other derivatives (Lamartina et al. 2018). Thyroidectomy is invasive as the entire thyroid gland is removed which can cause other potential complications such as hypocalcemia, hoarseness, and nerve damages (Chahardahmasumi et al. 2019; Christou and Mathonnet 2013). Therefore, novel approaches toward establishing minimally invasive methods are desired, preferably if a significant portion of the thyroid gland can remain intact.

Carbon nanotubes (CNTs) represent a unique class of nanomaterials characterized by tunable mechanical, electromagnetic, optical, and thermal properties (Simon et al. 2019; Alshehri et al. 2016). These characteristics have been explored greatly in biomedicine, including their applications in cancer therapy (Guo et al. 2015; Moon et al. 2009; Kafa et al. 2016; Robinson et al. 2010), tissue engineering (Lovat et al. 2005; Ren et al. 2017; Lorite et al. 2019), biosensing (Tilmaciu and Morris 2015; Sun et al. 2019; Alvarez et al. 2020), and imaging (Gong et al. 2013; Welsher et al. 2011; Hong et al. 2012). Multiwalled CNTs (MWCNTs) are made up of multiple concentric graphite-like layers, characterized by a large surface area with a very high aspect ratio (diameter vs. length). They are easily amendable to chemical modification allowing for extensive surface conjugation of different biological molecules of interest, such as drugs, antibodies, peptides, oligonucleotides, and fluorophores (Gu et al. 2011; Panczyk et al. 2016; Chakravarty et al. 2008; Lee et al. 2017). In addition to their cargo-like characteristics, MWCNTs have spectacular absorption properties that in turn can generate a tremendous amount of heat in extreme near-field fashion in a short time (femtoseconds] upon laser light exposure (Zhou et al. 2009; Liang et al. 2016; Sobhani et al. 2017). Accordingly, they could preferentially be brought to the proximity of targeted cell surfaces by the aid of specific ligands, then irradiated with light which would subsequently cause thermal necrosis of the tumor while inflicting minimal side effects to non-targeted regions. Such photothermal protocols have been widely investigated and shown to be a minimally invasive therapeutic method (Zhou et al. 2009). As such, the application of nanoparticle-mediated photothermal therapies has been investigated to assess different types of tumors, including those at the prostate (Lee et al. 2017; Rastinehad et al. 2019; Jin et al. 2016), breasts (Li et al. 2020; Ashkbar et al. 2020), melanoma (Chen et al. 2018; Bear et al. 2013), and more (Dotan et al. 2016) with successful ablation outcomes.

For successful photothermal therapy, three key criteria/challenges need to be addressed. First is predictive pre-operational planning. To address this issue, we have developed a theoretical model to predict the thermal accumulation and dissipation during laser ablation in vivo. Using COMSOL-based modeling, we were able to successfully optimize the experimental parameters for our laser-directed MWCNT treatment

conditions. Second criteria is the real-time monitoring of tumor ablation and the precise control of the temperature at the targeted region (Bastiancich et al. 2020), which continues to remain as one of the greatest challenges of any nanoparticle-assisted tumor photothermal ablation. Finally, the treatment strategy should ensure a complete tumor ablation response with minimal side effects. Despite the use of lasers in the near-infrared (NIR) wavelength range, adjacent nearby tissues themselves with natural chromophores also absorb light, which not only limits the penetration depth but may also cause damage to the tissues themselves.

To demonstrate the feasibility of the three-step process outlined above, we have utilized MWCNTs conjugated with thyroid stimulating hormone receptor (TSHR) antibodies, which further augmented the enhanced permeability and retention (EPR) effect and led to the increased accumulation of the CNTs within the TSHR-expressing BCPAP tumor xenografts. By integrating TSHR targeting strategies with appropriate laser ablation protocols (4.5 W over 2 min) optimized from the simulated models, we were able to induce complete tumor ablation of our preclinical PTC animal model while minimizing non-specific damage and deferring recurrence. Therefore, as a cancer therapy regimen, one can readily accept the benefits offered by photo-activated MWCNTs, specifically their thermal generating properties, minimal invasiveness, high specificity via targeting moieties, and precise temperature control (Zhao et al. 2021; Zou et al. 2016; Han and Choi 2021).

Materials and methods

Preparation of carboxylated MWCNTs

Carboxylic acid functionalized MWCNTs (MWCNT-COOH) ((extent of labeling: < 8%)) 9.5 nm diameter × 1.5 μm length) were purchased Sigma-Aldrich (St. Louis, MO, USA). 200 mg of the MWCNT-COOH were refluxed in 20 mL, 3:1 *v*/*v* mixture of concentrated sulfuric acid (98%, Sigma-Aldrich) to nitric acid (70%, Sigma-Aldrich) for 24 h at 80 ℃. Once the reflux was complete, the oxidized MWCNT solution (oxMWCNT) was repeatedly washed to remove the residual acid and resuspended in MilliQ grade water to obtain the final stock concentration of 1 mg/mL.

Antibody modification

Thyroid specific hormone receptor antibodies (αTSHR, from Abcam, Waltham, MA) and IgG antibodies from human serum (IgG, Sigma-Aldrich) were partially modified with the Traut's reagent (Thermo Fisher Scientific, Waltham, MA, USA) to convert primary amine groups to thiols according to the manufacturer's instructions with slight modifications. In short, 1:10 molar ratio of the antibody to Traut's reagent (20 μL of 1 mg/mL antibodies with 2 μL of 0.1 mg/mL Traut's reagent dissolved in PBS supplemented with 5 mM EDTA) were mixed and incubated for 60 min at room temperature. After incubation, buffer exchange was performed using a centrifugation column (cutoff of 30 kDa).

Antibody MWCNT conjugation

First, the carboxylic acid groups on the oxMWCNT were activated using carbodiimide chemistry. Briefly, 0.5 mL of 0.2 mg/mL of oxMWCNT were diluted equivalent volume

of 0.1 M 2-(N-morpholino) ethanesulfonic acid buffer, pH 6 (MES, Sigma-Aldrich) to a final concentration of 0.1 mg/mL. 100 µL of 50 mM of 1-ethyl-3-(3-dimethylaminopropyl) carbodiimide hydrochloride (EDC, Sigma-Aldrich) and 100 mM of sulfo-N-hydroxysulfosuccinimide (NHS, Sigma-Aldrich) in MES buffer were sequentially added dropwise to the oxMWCNT solution and conjugation proceeded at room temperature for 30 min. After washing excess EDC/NHS, 50 µL of 20 mM of both maleimide-PEG_{5000}-NH_2 and Cy5.5-PEG_{5000}-NH_2 (Nanocs Inc, New York, NY) in 1 mM PBS (pH 7) were added and conjugation reaction proceeded at room temperature for 1 h. Subsequently, the thiolated antibody of interest was added and incubated overnight at 4 ℃. On the next day, the mixtures were centrifuged three times at 20,000 g for 1 h and washed in MilliQ grade water. Finally, the conjugated MWCNTs were resuspended in MilliQ grade water until further use. The formulations of functionalized MWCNTs will be referred to as αTSHR;Cy5.5-MWCNT for the αTSHR-conjugated MWCNTs and IgG;Cy5.5-MWCNT for the IgG conjugated MWCNTs.

Characterization of the carbon nanotubes

The different formulations of carbon nanotubes were characterized by their absorbance, Fourier transform infrared (FT-IR) spectroscopy, and zeta potential measurements according to the manufacturer's instructions. The near-infrared (NIR) absorbance of the CNTs between 200 and 1350 nm was measured using Cary 5000 (Agilent, Santa Clara, CA). The presence of Cy5.5 on the CNTs was confirmed using DS-11 FX + Spectrophotometer from DeNovix (Wilmington, DE). Spectrum Two FT-IR spectrometer (PerkinElmer, United States) was used to identify the presence of carboxylic acid on the CNTs. NanoBrook Omni (Brookhaven Instruments, Holtsville, NY,) was used to obtain the zeta potential of the CNTs based on the dynamic light scattering (DLS) technique. Raman spectrums of the different samples were obtained using the inVia confocal Raman microscope (Renishaw, Gloucestershire, United Kingdom). The transmission electron microscopy (TEM) images were collected using the FEI Tecnai G2 Spirit Twin 120 kV Cryo-TEM located at the Facility for Electron Microscopy Research at McGill University.

Cell culture

TSHR-positive, human papillary thyroid cancer cell line BCPAP was acquired from the American Type Culture Collection (ATCC, Manassas, VA) and cultured in RPMI-1640 medium supplemented with 10% heat-inactivated fetal bovine serum (FBS), 1% penicillin–streptomycin and Plasmocin™ prophylactic (InvivoGen, San Diego, CA). Cultures were maintained in a humidified atmosphere with 5% CO_2 at 37 °C and routinely tested for mycoplasma contamination. Cells were subcultured once they reached approximately 80% confluency.

In vitro *ablation of human thyroid cancer cells*

BCPAP cells were seeded on 48-well chambers at a density of 5×10^4 cells per well. Following 24 h, different concentrations of the unlabeled carbon nanotubes (0.1, 0.39, 1.56, 3.25, 6.25, 12.5, 25, 50, and 100 µg/mL) were added to the wells. The cells were then either treated with the 808 nm wavelength, 4.5 W laser for 30 s followed by PBS

washes or left untouched before evaluating the cell viability with thiazolyl blue tetrazolium bromide (MTT, M2128, Sigma-Aldrich) assay according to the manufacturer's protocols. Briefly, 5 mg/mL of MTT solution in phenol red-free RPMI-1640 medium was filtered through 0.22 μm syringe filter, added to the treated cells at a final concentration of 0.5 mg/mL, and were incubated for 3 h inside cell culture incubator with 5% CO_2 at 37 °C. After 3 h, the crystals were dissolved with 100 μL of DMSO and absorbance was read at 570 nm.

Confocal microscopy evaluation of CNTs on TSHR-positive cell lines

BCPAP cells were seeded on 8-well Nunc™ Lab-Tek™ II Chamber Slide™ System (Thermo Fisher Scientific) at a density of 5×10^4 cells per well. On the next day, the cells were fixed with 4% formaldehyde (prepared from the paraformaldehyde stock) for 15 min then treated with 100 μL of αTSHR;Cy5.5-MWCNT and IgG;Cy5.5-MWCNT for an hour. Once the incubation was completed, the cells were counterstained with 4′,6-diamidino-2-phenylindole (DAPI, from Thermo Fisher Scientific) for 15 min. During the entire fixation and staining processes, the cells were washed with fresh PBS. The images were acquired using LSM800 Airyscan Confocal Microscope (Carl Zeiss, Inc., Oberkochen, Germany), using the excitation/emission wavelengths of 358/461 and 684/710 nm for DAPI and Cy5.5, respectively.

BCPAP xenograft mouse model

Immunodeficient BALB/c nude mice between 5–6 weeks old were purchased from Charles Rivers (Montreal, Canada) for in vivo studies. The mice were acclimated for a week before the start of the study and were maintained at standard conditions: 25 ± 2 ℃, 50 ± 10% relative humidity, and 12 h light/12 h dark cycle. All mice were fed with sterilized standard mouse chow and water ad libitum. After the acclimatization periods, 200 μL of 7.5×10^6 BCPAP cells suspended in 1:1 PBS:Matrigel (Catalog 356231, Corning, Tewksbury, MA, USA) were injected into the right flank regions of the nude mice. Tumor sizes were monitored biweekly with a digital caliper according to the formula $\text{width}^2 \times \text{length} \times 0.5$. Once the tumor volumes reached 150–200 mm^3, the mice were randomly assigned to different treatment groups. Mice were euthanized once the tumor size reached > 2000 mm^3 in size. All in vivo protocols were verified according to the guidelines of the Lady Davis Institute/McGill University.

Treatment schedule and biodistribution

To establish the treatment schedule, 9 BCPAP tumor-bearing mice were prepared according to the outlined protocol. Three experimental groups—(i) negative control group with PBS injection, (ii) those receiving αTSHR;Cy5.5-MWCNT, and (iii) those receiving IgG;Cy5.5-MWCNT were prepared. For each mouse, either PBS or 1 mg/kg of respective CNT formulations (αTSHR;Cy5.5-MWCNT and IgG;Cy5.5-MWCNT) was injected intravenously. The mice were then monitored for up to a week and the Cy5.5 fluorescence signals from the injected nanoparticles were measured at 24 h, 48 h, 72 h, and 144 h post-injection using the In Vivo Imaging Solutions (IVIS) Spectrum (PerkinElmer, United States) with the excitation/emission filters at 675/720 nm.

Furthermore, 9 additional BCPAP tumor-bearing mice were used to evaluate the biodistribution profiles of the CNTs. Similar to the previous experiment the mice were determined into three experimental groups and were injected with PBS or 1 mg/kg of respective CNTs (αTSHR;Cy5.5-MWCNT and IgG;Cy5.5-MWCNT). Twenty-four hours after the mice were euthanized, major organs including the tumor, liver, kidneys, spleen, heart, and lungs were collected for Cy5.5 (i.e., MWCNT) biodistribution analysis using the IVIS system.

Thermal modeling

A 2D axisymmetric physical model for spherical tumors surrounded by adjacent healthy tissues and epidermal layer from the above was designed in a cylindrical form (See Additional file 1: Data 1). The model's surface was assumed to be illuminated by an external collimated Gaussian laser beam with a wavelength of 808 nm. The commercially available FEM package (COMSOL Multiphysics 5.6 with the Bioheat module; Burlington, MA) was used to develop a finite element model to predict the tumor tissue's transient temperature response upon laser exposure. The thermal behavior of tissue was simulated by applying the Penne's-Bioheat transfer equation (Pennes 1948):

$$\rho C_p \frac{\partial T}{\partial t} = \nabla(k\nabla T) + \rho_b C_b \omega_b (T_b - T) + Q_{met} + Q_{laser}. \quad (1)$$

The initial condition was obtained as the steady-state solution of the Bioheat equation in the absence of the external laser source, which corresponds to the body's physiological parameters at the surface temperature of T = 33 ℃ and the core temperature of T = 36.6 ℃ (Reitman 2018; Gordon 2017). The heat transfer at the boundary between the top surface and the surrounding environment was subjected to the convective heat flux mechanism according to Eq. 2:

$$-n\,(-k\nabla T) = h\,(T_{ext} - T). \quad (2)$$

The characteristics of the external laser source, the optical properties of the biological tissues, and the MWCNTs used in this study are described further in Additional file 1: Data 1.

Tumor ablation. The experimental groups for the tumor ablation studies were defined as follows: negative controls (i) injected with PBS, (ii) laser only, (iii) laser + IgG;Cy5.5-MWCNT, and positive targeted (iv) laser + αTSHR;Cy5.5-MWCNT. Each group included five mice. The experimental mice were intravenously administered their respective treatments 24 h before the laser treatment. During the entire laser treatment procedure, the mice were induced and maintained under general anesthesia using isoflurane and the body temperature was maintained using a thermal heat pad. Once under anesthesia, each mouse received laser irradiation—808 nm 4.5 W—for 2 min. The surface temperature was monitored in real-time using the FLIR C2 Compact Thermal Imager (FLIR Systems, Wilsonville, OR). Once the treatment was completed the irradiated area was treated with topical ointments using Q-tips to assist in scar healing.

Immunohistochemistry

The different treatment groups (negative control injected with PBS, laser only, laser + IgG;Cy5.5-MWCNT, and laser + αTSHR;Cy5.5-MWCNT) were evaluated with hematoxylin and eosin (H&E) and human mitochondrial staining. First, the BCPAP tumor samples were collected at 24 h and 5 weeks post-laser treatment and fixed in 10% formaldehyde before being embedded in paraffin blocks. Subsequently, the 4-μm sections were stained with H&E or antibody against human mitochondria (α-Mitochondria antibody [clone 113-1], from Abcam, Waltham, MA) at a dilution of 1:1000. Three independent images were captured, and the amount of mitochondrial staining was quantified using the Positive Pixel Count v9 algorithm on Aperio ImageScope (Leica Biosystems, ON, Canada).

Statistical analysis

Data are expressed as mean ± standard deviation (SD). The Student's t-test was used to compare the localization of αTSHR and IgG-labeled CNTs and the human mitochondrial staining. One-way repeated measures ANOVA with Tukey's post hoc analysis was used to compare multiple experimental groups (GraphPad Prism 8.0, San Diego, CA). Probability (p) values of < 0.05 were considered statistically significant.

Results

Characterization of the MWCNTs

The degree of surface functionalization (Jain et al. 2011; Allegri et al. 2016; Mohammadi et al. 2020) (e.g., COOH) and length (Sato et al. 2005; Hamilton et al. 2013, 2018; Fujita et al. 2020) of the MWCNTs have an important effect relating to potential cytotoxicity. Although a consensus has not been reached, it is generally believed that a higher degree of MWCNTs functionalization and MWCNTs of shorter length alleviate the potential cytotoxicity elicited by CNTs both in vitro and in vivo (Zhao et al. 2021). Therefore, we have further oxidized the MWCNTs to introduce additional carboxylic groups on the surface of the MWCNTs which led to increased biocompatibility and hydrophilicity as well as improved surface covalent conjugation. We introduced a mixture of heterobifunctional PEG crosslinkers containing either maleimide or Cy5.5 to the surface of the oxidized MWCNTs, followed by the addition of Traut's reagent-modified thiolated-TSHR or IgG antibodies. The summary of MWCNT preparation, including oxidation, PEGylation, and antibody labeling is summarized in Fig. 1A. Following the conjugation, the different formulations of CNTs were characterized by Fourier transform infrared spectroscopy [FT-IR), Raman spectroscopy, UV-Vis spectroscopy, and dynamic light scattering [DLS) [Fig. 1B). Using FT-IR, we were able to confirm the presence of -COOH groups with a noted band at 1750 cm^{-1}. The PEG-Cy5.5 conjugation to the MWCNTs was confirmed with UV-Vis spectroscopy, identified by a small absorbance peak at ~ 680 nm, that corresponds to Cy5.5. Raman spectroscopy was used to identify the D and G peaks around 1300 and 1600 cm-1, respectively, and the presence of smaller peaks that represent the presence of different bonds that are present on the MWCNTs following conjugation. The surface conjugation of various moieties was also confirmed by the changes in their zeta potentials with the unmodified CNT-COOH [resuspended in Milli-Q water supplemented with 0.1% Tween20), oxMWCNTs, αTSHR;Cy5.5-MWCNT

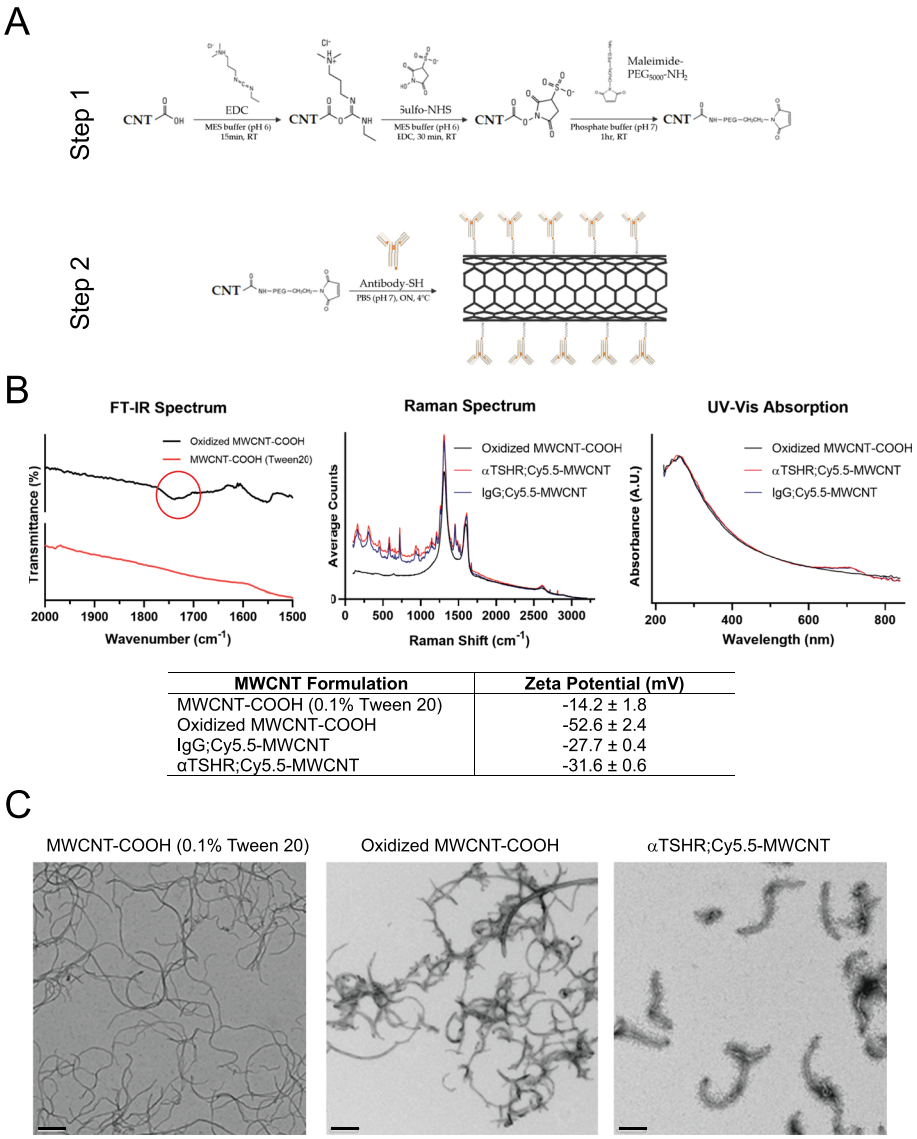

MWCNT Formulation	Zeta Potential (mV)
MWCNT-COOH (0.1% Tween 20)	-14.2 ± 1.8
Oxidized MWCNT-COOH	-52.6 ± 2.4
IgG;Cy5.5-MWCNT	-27.7 ± 0.4
αTSHR;Cy5.5-MWCNT	-31.6 ± 0.6

Fig. 1 Overall conjugation chemistry and characterization of the CNT conjugates. **A** The two-step conjugation of anti-TSHR antibodies onto the surface of CNTs. Step 1: The heterobifunctional maleimide-PEG_{5000}-NH_2 crosslinker is conjugated onto the EDC/NHS activated MWCNT surface. Step 2: The thiol group on anti-TSHR antibodies reacts with the maleimide terminal end of the CNT-PEG_{5000}. **B** The characterization of different CNT formulations with FT-IR, Raman spectrum, and UV–Vis spectroscopy. A small peak, indicated by a circle, near 1750 cm^{-1} corresponding to carboxylic acids is observed in FT-IR spectra after CNT oxidation. Conjugation of antibodies and Cy5.5 is confirmed with Raman spectrum and UV–Vis spectroscopy, respectively. **C** TEM images of different CNT formulations. Scale bar sizes represent 200 nm

and IgG;Cy5.5-MWCNT measured − 14.2 ± 1.8, − 52.6 ± 2.4, − 31.6 ± 0.6 and − 27.7 ± 0.4 mV, respectively. Transmission electron microscopy (TEM) images were also obtained which showed unmodified MWCNTs, length compared to oxidized MWCNTs had decreased but importantly maintained their tube-like structural integrity (Fig. 1C). EDS elemental analysis also confirmed the conjugation of the antibody onto the MWCNTs, through the presence of nitrogen atoms (data not shown). These MWCNTs formulations were used for all subsequent experiments described below.

In vitro cell viability and confocal microscopy

Previously, we demonstrated that MWCNTs labeled with specific targeting ligands and laser treatment can induce selective cell photoablation upon binding of αTSHR-targeted BCPAP and αPSMA-MWCNT LNCaP cells in vitro (Lee et al. 2017; Dotan et al. 2016). We wished to complement these studies by assessing the also potential cytotoxic effects and ablative potential of non-targeted MWCNTs, by incubating the TSHR-expressing BCPAP cells with increasing concentrations of oxMWCNTs. Based on the MTT assay, we observed the viability of BCPAP cells was minimally affected with up to 100 μg/mL of oxMWCNTs in solution (Fig. 2A). We then assessed the bulk photothermal effects on cell viability with the increasing oxMWCNT concentrations coupled to laser irradiation and by comparing the viability of cells under two conditions: MWCNTs in solution or MWCNTs removed by washing prior to the 30-s irradiation of 4.5 W 808-nm laser. The viability of cells exposed to oxMWCNTs during irradiation decreased with increasing concentrations of MWCNTs ($p = 0.03$) while the viability of cells where MWCNTs were removed before irradiation was largely unaffected. These results revealed that our oxidized MWCNT preparation had a minimal cytotoxic effect and that cellular ablation required both MWCNTs and light exposure.

We also observed the selective binding of αTSHR;Cy5.5-MWCNTs on the surface of BCPAP cell lines (Fig. 2B). Confocal microscopy imaging of BCPAP cells incubated with αTSHR;Cy5.5-MWCNTs exhibited stronger fluorescence signals, while a minimal signal was observed from the cells incubated with non-specific IgG;Cy5.5-MWCNT. We assessed the fluorescence intensity for the binding of the two MWCNT formulations and found αTSHR;Cy5.5-MWCNTs had a 2.84 fold signal enrichment ($p = 0.0287$) (Fig. 2C), demonstrating the specific targeting toward TSHR-expressing BCPAP cells.

Biodistribution and selective tumor localization and retention of αTSHR-MWCNTs

In vivo studies were designed to evaluate the biodistribution profiles to establish the treatment schedule of the different formulations of CNTs. We first assessed the biodistribution of two MWCNT formulations, αTSHR;Cy5.5-MWCNTs and IgG;Cy5.5-MWCNT, in BCPAP xenografted tumor mice by tail vein injection of 1 mg/kg of each MWCNT conjugate. Organ-based analysis showed that the strongest Cy5.5 signal was observed in the tumor followed by the kidneys and the liver 24 h post-intravenous injection (Fig. 3A). Importantly, while the fluorescence signals between the two MWCNT formulations were similar across the organs examined, the active-targeting αTSHR;Cy5.5-MWCNTs had preferential accumulation at the tumor ($p = 0.038$) compared to the IgG;Cy5.5-MWCNT when normalized to the PBS-injected mice (Fig. 3B).

Subsequently, the treatment schedule (i.e., laser exposure) was determined by assessing the distribution and retention of the αTSHR targeted of the MWCNTs at the tumor. Similarly, 1 mg/kg of the two different formulations of MWCNTs were injected intravenously and monitored for accumulation in the tumor for up to a week. It was observed that the maximal fluorescence signal at the tumor was reached between 24- and 48-h post-injection (Fig. 3C). The signals started to diminish at 72 h and by 144 h have declined to 51% and 62% of the maximal peak values of IgG-MWCNT and αTSHR-MWCNTs, respectively. Similar to the results from the biodistribution studies, the

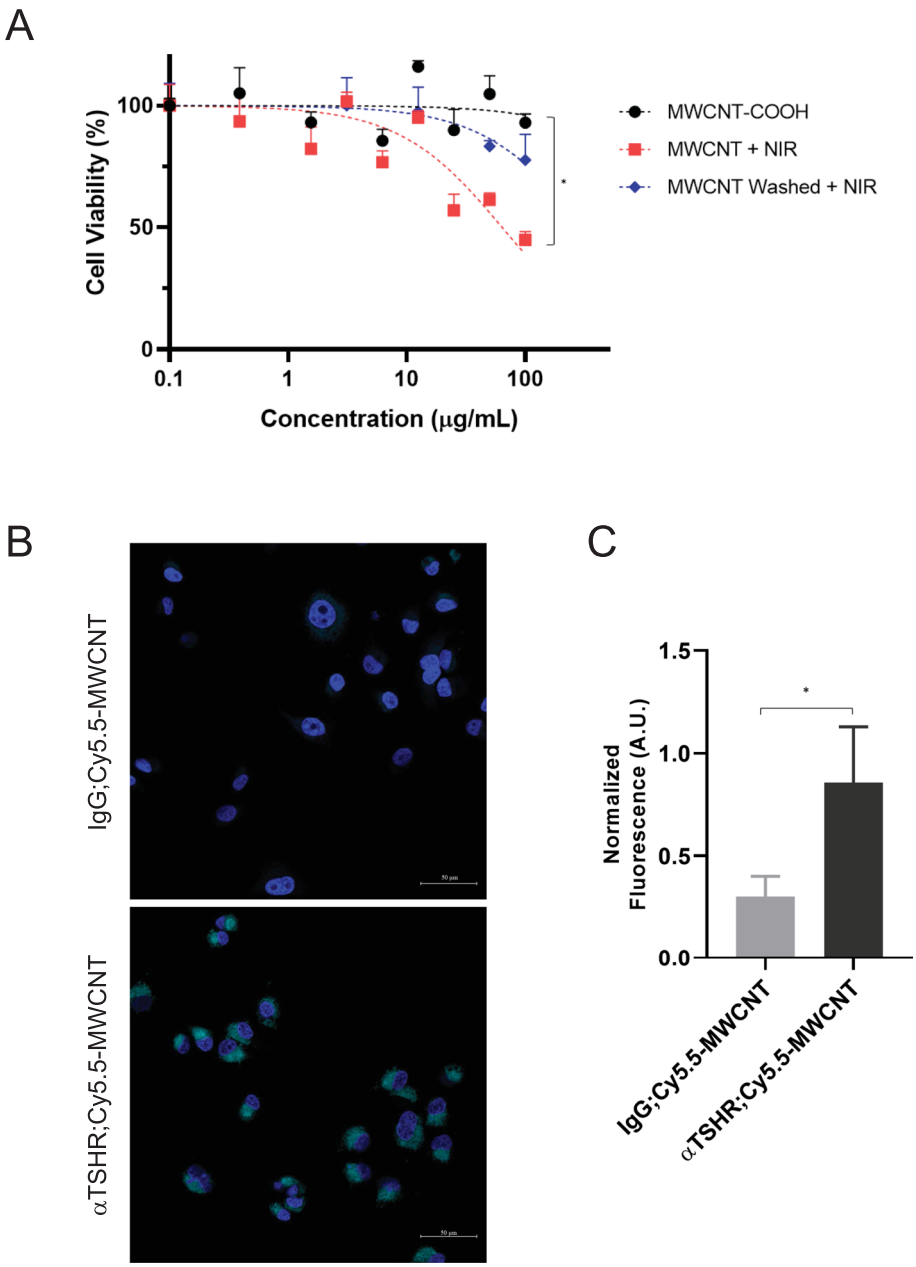

Fig. 2 In vitro cell ablation and confocal microscopy. **A** In vitro cell ablation was evaluated with the MTT assay, using a range of MWCNT concentrations (0.1, 0.39, 1.56, 3.25, 6.25, 12.5, 25, 50, and 100 μg/mL). CNT-COOH (solid black circle) by itself had minimal influence on cell viability, as over 90% of cells remained viable at concentrations up to 100 μg/mL. On the other hand, cell viability decreased significantly after laser irradiation ($p = 0.03$) (red square). Nevertheless, if CNTs were removed before laser irradiation (blue diamond), cell viability was not affected significantly ($p = 0.55$). **B** TSHR-positive BCPAP papillary thyroid carcinoma cells were incubated with IgG; Cy5.5-MWCNT and αTSHR; Cy5.5-MWCNT. Selective binding of the αTSHR-labeled CNTs on the cell surface was observed. Scale bar = 50 μm. **C** αTSHR; Cy5.5-MWCNT-labeled cells had 2.84 fold enrichment of Cy5.5 signal at the cell surface over the IgG IgG; Cy5.5-MWCNT-labeled cells ($p = 0.0287$)

αTSHR;Cy5.5-MWCNT injected mice showed significantly higher fluorescence at the tumor than those injected with IgG;Cy5.5-MWCNTs across all time points examined (24 h, $p = 0.046$; 48 h, $p = 0.049$; 7 2 h, $p = 0.019$; and 144 h, $p = 0.043$) (Fig. 3D). These results not only highlight the selective targeting, but also the prolonged retention of

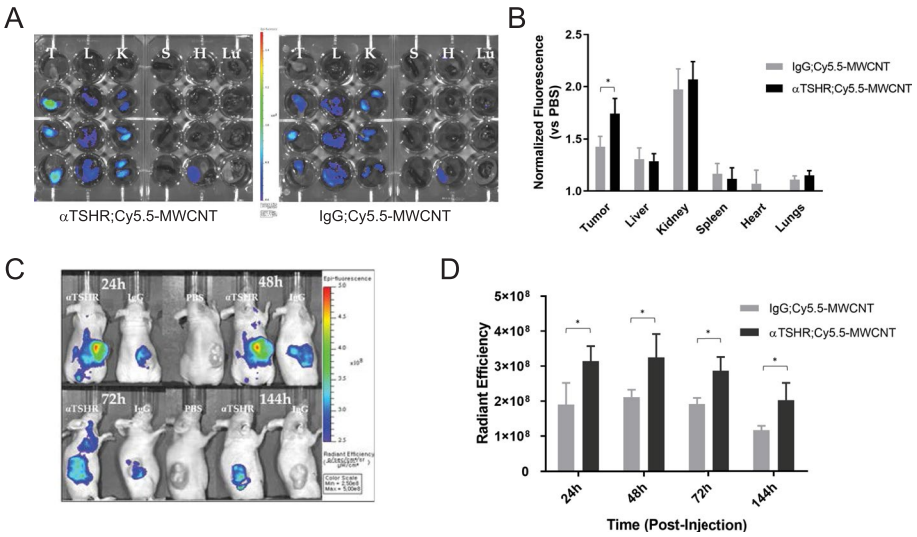

Fig. 3 In vivo tumor accumulation and biodistribution profiles. **A** IVIS was used to monitor the tumor and organ biodistribution profiles of αTSHR; Cy5.5-MWCNT and IgG; Cy5.5-MWCNT 24 h post-intravenous injection, where T = tumor, L = liver, K = kidneys, S = spleen, H = heart, Lu = lungs. **B** Significant improvement in the accumulation of the αTSHR-labeled CNTs was observed in the tumor (1.22-fold increase, $p = 0.0376$), while fluorescence at other major organs remained unchanged. **C** The accumulation of CNTs at the tumor post-intravenous injection for a week. **D** Enhanced accumulation of αTSHR; Cy5.5-MWCNT was observed at the tumor throughout the observed period compared to IgG; Cy5.5-MWCNT ($p = 0.046$, 0.049, 0.019, and 0.043 for 24, 48, 72 and 144 h, respectively)

αTSHR;Cy5.5-MWCNTs. According to our calculations, each MWCNT molecule would have up to 1000 αTSHR antibodies conjugated on its surface. It has been estimated that there are approximately 5000 TSHR expressed at the surface per cell (Rees Smith et al. 1988). Therefore, the enhanced retention of the targeted nanoparticles at the tumor site is a result of the favorable binding kinetics of the high-density antibody-labeled MWCNTs to the respective receptors on each cell. Overall, based on these results we chose 24 h post-injection as the maximal targeted MWCNT accumulation time point at which we would perform our laser-directed tumor ablation experiments.

Thermal modeling

The success of tumor ablation will be largely dependent on the distribution of thermal energy generated upon laser irradiation. A critical temperature threshold needs to be reached for effective tumor ablation; moreover, the distribution of temperature also needs to be managed to minimize causing collateral tissue damage. As infrared thermal cameras are limited to measuring only the surface temperature, it has been a challenge to accurately monitor the temperature changes in the intratumoral space. Accordingly, we have developed an algorithm using COMSOL simulation to predict the intratumoral temperature upon laser irradiation based on the following parameters: laser power characteristics, optical properties of the MWCNTs, and thermal responses of the tumor and surrounding tissues. Temperature modeling was carried out based on a hypothetical 7-mm-diameter spherical tumor surrounded by a 0.5-mm-thick epidermal skin layer on top and background tissue at the bottom. Assessed tissue parameters included density,

specific heat capacity, thermal conductivity, blood perfusion, and metabolic heat of the tumor and the background tissue (see Additional file 1 Data 1, Table S2).

First, the theoretical average temperature of the tumor surface upon laser irradiation (NIR only, 808 nm wavelength, 120 s duration) was calculated by taking the integral of the laser-exposed region using three different laser outputs of 2 W, 4.5 W, and 7 W (Fig. 4A). We next assessed tumor surface temperatures simulated with localized targeted CNTs and receiving NIR treatment, with the same laser outputs as described above. The fraction of the tumor occupied by the injected MWCNTs was calculated using the percentile estimation from Wilhelm et al.'s (Wilhelm et al. 2016) meta-analysis, the amount of the nanoparticles injected (1 mg/kg), the true density of the MWCNTs provided by the manufacturer (2.04–2.4 g/cm^3), and the volume of the tumor. The surface temperature of CNT modeling with 4.5 W and 7 W of output power showed a rapid increase in temperature vs NIR-only, reaching 45 ℃ in less than 30 s following laser irradiation; whereas 2 W + CNT or NIR-only conditions needed a significantly longer time (> 1 min) (Fig. 4B). Based on the visualization of the 3D temperature distribution of the intratumoral space, we observed that only the upper half of the tumor had increased temperature in 2 W + CNT modeling conditions, whereas 4.5 W and 7 W heating from CNT irradiation was extended throughout the tumor (Fig. 4C). Figure 4D illustrates

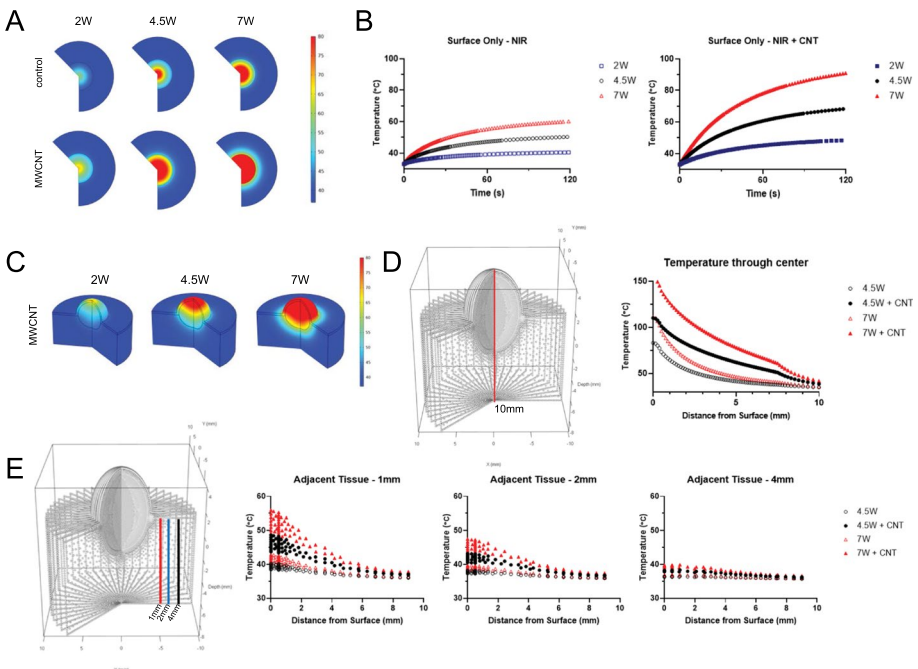

Fig. 4 Predicted intratumoral temperature profiles. **A** Visualization of the predicted surface temperatures in the tumors with or without the nanoparticle injection exposed to 2 W, 4.5 W, and 7 W 808 nm wavelength laser. **B** The average predicted tumor surface temperature across, with and without CNTs, over 120 s with exposure to the 808 nm wavelength laser. **C** The 3D temperature distribution of the tumor upon photothermal ablation of CNT injected conditions, across the three laser power outputs. **D** Sectional illustration depicting a 10 mm cross-section of data points through the intratumoral space together with the graphical representation of 4.5 W and 7 W, in the presence and absence of CNTs. **E** Section illustration depicting data points, 1 mm, 2 mm, and 4 mm adjacent to the tumor mass together with graphical representation, of temperature over the 9 mm distance from the surface

the data points of temperature captured and graphically represents 4.5 and 7 W of laser power with and without the presence of CNTs. In the presence of CNTs, both 4.5 W and 7 W of laser caused temperature to reach above 50 ℃ throughout the 7 mm tumor. However, while 7 W was able to generate critical heat through the whole of the tumor, heat also radiated beyond the tumor into the background tissue. By measuring the temperature of the adjacent, normal tissue at 1 mm, 2 mm, and 4 mm away from the tumor periphery, we observed excessive temperature increases 2 mm into the normal tissues (> 50 ℃ at 1 mm and > 45 ℃ at 2 mm) in the model receiving 7 W of laser power (Fig. 4E). Based on this modeling, tumors receiving MWCNTs and 4.5 W radiation would obtain both the critical and manageable temperature threshold in the tumor and its adjacent tissue margins. As such, we used this information to establish the settings of 4.5 W of total laser power over a 2-min period as the photoablation protocol of the xenografted tumors.

αTSHR-MWCNT targeted tumor photoablation animal studies: selectivity and efficacy

Twenty-four hours after αTSHR;Cy5.5-MWCNT, IgG;Cy5.5-MWCNT, or PBS administration, BCPAP tumor-bearing mice were irradiated with an 808 nm NIR laser delivering 4.5 W laser power for 2 min to the tumor site. To validate our thermal modeling, the tumor surface temperature was monitored with a FLIR thermal camera during the laser treatment (Fig. 5A). The αTSHR;Cy5.5-MWCNT formulation generated higher temperatures at the tumor site upon laser irradiation compared to the PBS-injected or IgG:Cy5.5-MWCNT control groups receiving the laser treatment (Fig. 5B). Specifically, animals injected with αTSHR;Cy5.5-MWCNTs saw a temperature change of + 28 ℃ at the tumor surface (2 min) while those animals receiving the laser treatment without the CNTs saw a temperature change of + 17 ℃ ($p < 0.001$). These temperature increases are in line with our thermal modeling that predicted + 33 ℃ and + 17 ℃ for the αTSHR;Cy5.5-MWCNT and the NIR-only treatment cohort, respectively.

To study the treatment efficacy our tumor photothermal ablation studies were divided into three treatment cohorts: (i) PBS injection plus laser treatment, (ii) IgG;Cy5.5-MWCNT injection plus laser treatment, and (iii) αTSHR;Cy5.5-MWCNT injection plus laser treatment. We also included a PBS injection no treatment cohort of tumor-bearing animals. Immediately after tumor ablation, we observed a tightening of the skin where the laser treatment was performed followed by the formation of eschar a few days later (Additional file 2: Data 2). In mice that received just PBS plus laser treatment, tumors eventually regrew with the tumor volumes reaching 150–200 mm^3 by two weeks (the approximate size of the tumors at the time of treatment) and > 500 mm^3 by 3.5 weeks post-treatment (Fig. 5C). A similar tumor regrowth pattern was also observed in animals that received the non-specific IgG;Cy5.5-MWCNTs plus laser treatment regimen after 3.5 weeks. These results suggest that laser alone and/or non-specific accumulation of CNTs at the tumor site was insufficient to generate the heat needed to cause significant tumor ablation and prevent tumor recurrence. In contrast, mice that were injected with the targeted αTSHR;Cy5.5-MWCNT saw a significant reduction of tumor volume upon laser treatment at 5 weeks post the treatment (vs. IgG;Cy5.5-MWCNT, $p = 0.01$). We also assessed the regrowth of tumors, for which recurrence was defined as the point when tumors had grown beyond their initial size at the time of the treatment. In the

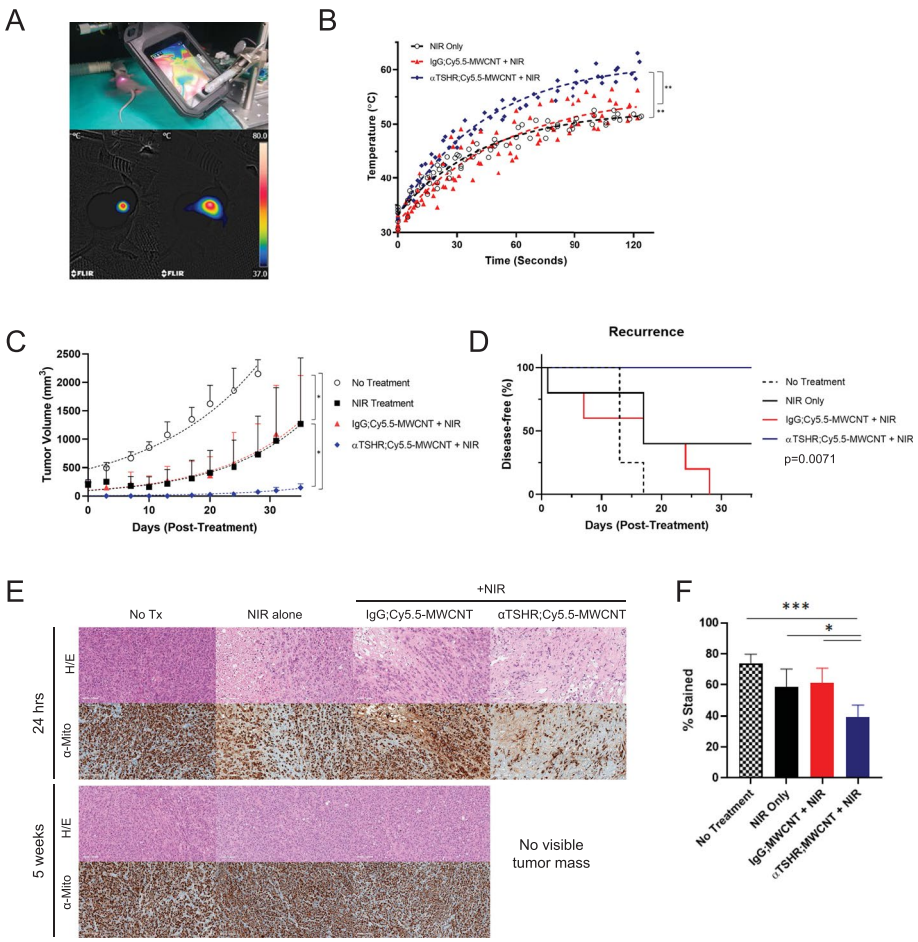

Fig. 5 In vivo temperature monitoring and xenograft tumor ablation. **A** The temperature of the surface of the tumor upon laser irradiation was monitored using FLIR thermal camera. **B** Documentation of the surface temperature of those injected with αTSHR; Cy5.5-MWCNT over other groups. A significant increase in temperature was observed ($p < 0.01$ for all). **C** The size of the tumor after laser irradiation was monitored for five weeks. Those that were administered with αTSHR; Cy5.5-MWCNT saw near-complete tumor ablation, while the other groups had tumor recurrence. **D** Survival outcomes were assessed by tumor size recurrence of the different treatment cohorts. **E** H&E staining and human mitochondrial staining of the tumors. Scale bar = 100 µm. **F** Quantification of the human mitochondrial staining, post 24 h irradiation. Those that received αTSHR;Cy5.5-MWCNT + laser treatment protocol saw a significant decrease in the mitochondrial staining signal ($p < 0.001$ vs. no treatments, $p < 0.05$ vs. NIR alone or IgG;Cy5.5-MWCNT), underscoring the selective ablation of the TSHR-targeted BCPAP tumors

αTSHR;Cy5.5-MWCNT cohort, suppression of tumor recurrence was defined as tumor sizes maintaining < 200 mm^3 volumes throughout 5 weeks of observations (Fig. 5D). Photothermal treatment with 2 W laser power output without CNTs was also evaluated, but the irradiation was not sufficient to cause complete tumor ablation as tumor regrowth was observed (Additional file 3: Data 3). These results match well with the interpretation of the predicted intratumoral temperature as insufficient temperature elevation around the tumor margins allowed for tumor recurrence.

Pathological evaluations of tumor tissue resected 24 h and 5 weeks post-laser treatment indicated that although some tissue damage can be inflicted by the laser in the PBS and IgG;Cy5.5-MWCNT conditions after 24 h, severe tumor ablation was observed only in the αTSHR;Cy5.5-MWCNT treatment regimen post-24 h followed by no observable

tumor mass after 5 weeks (Fig. 5E). Furthermore, upon staining for the human-specific mitochondrial marker to differentiate human BCPAP tumor cells vs. murine interstitial cells, we were clearly able to observe a decrease in the human mitochondrial expression in the tissue sections from the αTSHR;Cy5.5-MWCNT cohort ($p < 0.001$ vs. PBS, $p = 0.04$ vs NIR only, and $p = 0.02$ vs IgG;Cy5.5-MWCNT), providing more evidence that the targeted treatment protocol can induce significant and selective ablation of the targeted cells (Fig. 5F).

Several conclusions can be drawn from the αTSHR;Cy5.5-MWCNT targeted tumor photoablation. First, an adequate amount of MWCNTs had accumulated and was retained at the tumor site. Second, the amount of optical power delivered to the tumor site generated the critical temperature increase to cause irreversible necrotic damage to the tumor to prevent tumor recurrence. Finally, from a safety concern, αTSHR;Cy5.5-MWCNT treatment regime and other experimental conditions did not induce significant changes in the weights of the mice (Additional file 2: Data 2) or other observable adverse events, aside from epidermal scarring that initially appeared around the treatment region but quickly healed within a week.

Discussion

The advent of modern DNA sequencing of neoplasms has now clearly established the status of somatic mutations in cancer cells. Consortiums such as TCGA, International Cancer Genome Consortium, and COSMIC, have played an extremely important role in defining extensive genetic heterogeneity both inter- and intra-tumoral mutations of cancers. A result of the evolution of cancers is the acquisition of somatic mutations (Anderson et al. 2011; Berger et al. 2011; Lee et al. 2010; Pleasance et al. 2010a, 2010b; Puente et al. 2011), which in turn facilitate a selection process and drug resistance; many times induced by drug therapies themselves (Berger et al. 2011; Waltering et al. 2012; Kumar et al. 2011; Barbieri et al. 2012; Yu et al. 2012; Baca and Garraway 2012; Xu et al. 2013; Wu et al. 2012; Grasso et al. 2012; Hieronymus and Sawyers 2012). However, the treatment options for several cancer types still heavily rely on biological interventions. Surgical procedures are also optional, but they are invasive and often involve post-operative complications. On the other hand, physical agent therapies are immune to genetic alterations, as they deliver damaging entities to a targeted "area" or "field", and thus are lethal irrespective of cellular genetic background, as long as they are present within the targeted area. Thus, focal therapies such as external beam radiation therapy and thermal ablation have become alternative non-surgical procedures for further investigation (Berdelou et al. 2018). In particular, focal ablation using laser devices offers several advantages as they are also precise, predictable, and generate homogeneous ablation without inducing concomitant damage to structures surrounding the targeted tumor (Rastinehad et al. 2019). Therefore, using light-absorbing nanoparticles, such as MWCNTs, laser-based protocols can be further enhanced by lowering the optical power delivered to the tumor site.

To maximize the properties of the MWCNTs used in our tumor photoablation protocol, we functionalized the particles by oxidizing the surface of the MWCNTs and thereby enhancing their solubility and increasing the available carboxylic sites for TSHR antibody conjugation. Compared to the mice that were injected with a single intravenous

dose of target naïve (Cy5.5-MWCNT, data not shown) or non-specific IgG;Cy5.5-MWCNT, significantly more αTSHR;Cy5.5-MWCNTs had accumulated and were retained at the tumor site within 24 through 144 h observational window (Fig. 3D). Accordingly, while other groups have employed direct intratumoral injection strategies (Sobhani et al. 2017; Zhang et al. 2017) or administered higher doses (Robinson et al. 2010; Wang et al. 2020), we were able to use a lower amount of intravenous MWCNTs injections (1 mg/kg or ~ 25 μg total of MWCNT per injection) in this study. This serves as a strong asset as it is highly desired to use less amount of MWCNT injections to minimize any potential adverse systemic effects (Yan et al. 2019). As such, mice administered with 1 mg/kg of MWCNTs did not show any significant changes in their body weight or display any adverse events through five weeks following the laser treatment other than the temporal eschar formation.

Any photoablative treatment protocol should employ appropriate procedural planning, including thermal prediction, laser guidance, real-time monitoring of the tumor ablation, and post-operational follow-up are critical components required for any successful photothermal therapy. For example, in the pilot study for AuroLase®, the first ultra-focal tissue ablation therapy in clinical trials based on gold nanoshells-mediated photothermal therapy, the authors have combined magnetic resonance imaging (MRI)/ultrasound (US)-based stereotactic planning and temperature monitoring based on inserted sets of thermocouples to accurately follow the treatment protocols, resulting in successful treatment completion in 94% (15/16) of the enrolled patients without major adverse effects(Rastinehad et al. 2019). On the other hand, although numerous papers have shown efficient tumor ablation and infrared-based temperature monitoring (Robinson et al. 2010; Zhang et al. 2017, 2018; Lu et al. 2019), preoperational planning has often been overlooked in preclinical studies. Furthermore, while infrared thermal imaging has been used for real-time monitoring of temperature during laser ablation in preclinical studies (Jin et al. 2016; Chen et al. 2018; Bear et al. 2013), these temperature readings are superficial and can only read the temperature of the surface and do not accurately portray the internal core temperature where the actual tumor mass is located. Thermocouples (as done by Nanospectra for their pilot study in AuroLase®), computed tomography-based thermometry, or MR thermometry (Jin et al. 2016; West et al. 2019; Beik et al. 2019) could also be considered and are currently employed to complement the thermal monitoring process. Our experimental setup would also employ infrared thermal imaging to monitor the temperature, however, we developed a complementary algorithm based on the Bioheat equation (Eq. 1) to predict the temperature distribution of the tumor core. This would ensure that the critical temperature is achieved to ensure complete ablation of the tumor while simultaneously assessing the surrounding tissue area for non-specific damage (Fig. 4). For acute photothermal ablation, it has been demonstrated that an internal temperature of > 43 ℃ is critical for complete tumor remission while the duration or the fluence rate of the laser did not have significant effects (Nomura et al. 2020). By comparing the predicted surface temperature from the mathematical model with the experimental surface temperature (measured with the infrared thermal camera), we extrapolated the internal temperature to fit the predicted values to ensure complete tumor ablation. Thus, our optimized laser treatment protocol employed the

application of a 4.5 W laser treatment for 120 s, which would be sufficient to raise the internal tumor temperature above 43 ℃. In contrast, we also demonstrated that 2 W irradiation was insufficient as tumor recurrence was observed, whereas 7 W irradiation theoretically would cause significant damage to the adjacent tissue (Fig. 5B and Additional file 3: Data 3). Altogether, experimental evidence confirmed our modeling where the 4.5 W laser irradiation for 2 min in the αTSHR;Cy5.5-MWCNTs injected cohort was sufficient to completely ablate their tumors without displaying recurrence 5 weeks following irradiation (Fig. 5C). In the future, one can envision the application of a "closed-loop" system that would combine the computing power to model the thermal distribution throughout the tumor while simultaneously in real-time evaluating the laser-ablative process via controlled monitoring of temperature induction.

By first modeling temperature profiles of the tumor and the surrounding tissues in the presence of MWCNT and with various power outputs, we were able to predict treatment efficacy. As such, we successfully demonstrated that an antibody-MWCNT conjugate formulation against a receptor-specific cancer biomarker can selectively and passively accumulate and be retained at the tumor site for prolonged periods. Subsequently, these nano-targets can induce temperature-dependent cell ablation upon laser irradiation without significant tumor recurrence or any adverse outcome events. In conclusion, the results from this study could be used to improve the overall response to photothermal therapy and to develop preferred targeted-MWCNT protocols for the treatment of a diversity of cancers.

Supplementary Information

The online version contains supplementary material available at https://doi.org/10.1186/s12645-023-00184-9.

Additional file 1: Development of thermal modeling algorithm.

Additional file 2: Eschar formation following tumor ablation and monitoring.

Additional file 3: Photothermal ablation of BCPAP tumors using 2 W, 808 nm wavelength continuous laser for 2 minutes.

Acknowledgements
We thank Mr. David Liu at the Facility for Electron Microscopy Research of McGill University for help in microscope operation and data collection.

Author contributions
Conceptualization, SSL, MAT, and MP; formal analysis, SSL and FO; conducted experiments, SSL and FO; supervision, AGK, MAT, and MP; writing, review, and editing, SSL, FO, AGK, MAT, and MP. All authors have read and agreed to the published version of the manuscript.

Funding
Ministère de l'Économie, de la Science et de l'Innovation au Programme de soutien à la valorisation et au transfert volet 2B (PSVT2B). Guzzo Nano Research Corp (GNR), was the industry financing partner on this project—Project number: 17-19-PSVTB-41293.

Availability of data and materials
All data generated and analyzed during this study are available from the corresponding authors on reasonable request.

Declarations

Ethics approval and consent to participate
Animal ethics approval for this project was provided by McGill University Animal Compliance Office (2014-7463). All individuals that handled the animals received certified training.

Consent for publication
Not applicable.

Competing interests
MP and MAT are inventors of the following patent application, (WO2015070351), Bionanofluid for use as a contrast, imaging, disinfecting and/or therapeutic agent. MP and MAT are minority shareholders in Guzzo Nano Research Corp. (GNR). GNR has obtained a license agreement from McGill University to commercially develop the technology.

Received: 26 August 2022 Accepted: 28 March 2023
Published online: 05 April 2023

References
Allegri M, Perivoliotis DK, Bianchi MG, Chiu M, Pagliaro A, Koklioti MA et al (2016) Toxicity determinants of multi-walled carbon nanotubes: the relationship between functionalization and agglomeration. Toxicol Rep 3:230–243
Alshehri R, Ilyas AM, Hasan A, Arnaout A, Ahmed F, Memic A (2016) Carbon nanotubes in biomedical applications: factors, mechanisms, and remedies of toxicity. J Med Chem 59(18):8149–8167
Alvarez NT, Buschbeck E, Miller S, Le AD, Gupta VK, Ruhunage C et al (2020) Carbon nanotube fibers for neural recording and stimulation. ACS Appl Bio Mater 3(9):6478–6487
Anderson K, Lutz C, van Delft FW, Bateman CM, Guo Y, Colman SM et al (2011) Genetic variegation of clonal architecture and propagating cells in leukaemia. Nature 469(7330):356–361
Ashkbar A, Rezaei F, Attari F, Ashkevarian S (2020) Treatment of breast cancer in vivo by dual photodynamic and photothermal approaches with the aid of curcumin photosensitizer and magnetic nanoparticles. Sci Rep 10(1):21206
Baca SC, Garraway LA (2012) The genomic landscape of prostate cancer. Front Endocrinol 3:69
Barbieri CE, Baca SC, Lawrence MS, Demichelis F, Blattner M, Theurillat JP et al (2012) Exome sequencing identifies recurrent SPOP, FOXA1 and MED12 mutations in prostate cancer. Nat Genet 44(6):685–689
Bastiancich C, Da Silva A, Esteve MA (2020) Photothermal therapy for the treatment of glioblastoma: potential and preclinical challenges. Front Oncol 10:610356
Bear AS, Kennedy LC, Young JK, Perna SK, Mattos Almeida JP, Lin AY et al (2013) Elimination of metastatic melanoma using gold nanoshell-enabled photothermal therapy and adoptive T cell transfer. PLoS ONE 8(7):e69073
Beik J, Asadi M, Khoei S, Laurent S, Abed Z, Mirrahimi M et al (2019) Simulation-guided photothermal therapy using MRI-traceable iron oxide-gold nanoparticle. J Photochem Photobiol B 199:111599
Berdelou A, Lamartina L, Klain M, Leboulleux S, Schlumberger M (2018) Treatment of refractory thyroid cancer. Endocr Relat Cancer 25(4):R209–R223
Berger MF, Lawrence MS, Demichelis F, Drier Y, Cibulskis K, Sivachenko AY et al (2011) The genomic complexity of primary human prostate cancer. Nature 470(7333):214–220
Cabanillas ME, McFadden DG, Durante C (2016) Thyroid cancer. Lancet 388(10061):2783–2795
Chahardahmasumi E, Salehidoost R, Amini M, Aminorroaya A, Rezvanian H, Kachooei A et al (2019) Assessment of the early and late complication after thyroidectomy. Adv Biomed Res 8:14
Chakravarty P, Marches R, Zimmerman NS, Swafford AD, Bajaj P, Musselman IH et al (2008) Thermal ablation of tumor cells with antibody-functionalized single-walled carbon nanotubes. Proc Natl Acad Sci U S A 105(25):8697–8702
Chen W, Qin M, Chen X, Wang Q, Zhang Z, Sun X (2018) Combining photothermal therapy and immunotherapy against melanoma by polydopamine-coated Al2O3 nanoparticles. Theranostics 8(8):2229–2241
Christou N, Mathonnet M (2013) Complications after total thyroidectomy. J Visc Surg 150(4):249–256
Dotan I, Roche PJ, Paliouras M, Mitmaker EJ, Trifiro MA (2016) Engineering multi-walled carbon nanotube therapeutic bionanofluids to selectively target papillary thyroid cancer cells. PLoS ONE 11(2):e0149723
French JD (2020) Immunotherapy for advanced thyroid cancers—rationale, current advances and future strategies. Nat Rev Endocrinol 16(11):629–641
Fujita K, Obara S, Maru J, Endoh S (2020) Cytotoxicity profiles of multi-walled carbon nanotubes with different physicochemical properties. Toxicol Mech Methods 30(7):477–489
Gong H, Peng R, Liu Z (2013) Carbon nanotubes for biomedical imaging: the recent advances. Adv Drug Deliv Rev 65(15):1951–1963
Gordon CJ (2017) The mouse thermoregulatory system: its impact on translating biomedical data to humans. Physiol Behav 179:55–66
Grasso CS, Wu YM, Robinson DR, Cao X, Dhanasekaran SM, Khan AP et al (2012) The mutational landscape of lethal castration-resistant prostate cancer. Nature 487(7406):239–243
Gu YJ, Cheng J, Jin J, Cheng SH, Wong WT (2011) Development and evaluation of pH-responsive single-walled carbon nanotube-doxorubicin complexes in cancer cells. Int J Nanomed 6:2889–2898
Guo C, Al-Jamal WT, Toma FM, Bianco A, Prato M, Al-Jamal KT et al (2015) Design of cationic multiwalled carbon nanotubes as efficient sirna vectors for lung cancer xenograft eradication. Bioconjug Chem 26(7):1370–1379
Hamilton RF Jr, Wu Z, Mitra S, Shaw PK, Holian A (2013) Effect of MWCNT size, carboxylation, and purification on in vitro and in vivo toxicity, inflammation and lung pathology. Part Fibre Toxicol 10(1):57
Hamilton RF Jr, Tsuruoka S, Wu N, Wolfarth M, Porter DW, Bunderson-Schelvan M et al (2018) Length, but Not Reactive Edges, of Cup-stack MWCNT Is Responsible for Toxicity and Acute Lung Inflammation. Toxicol Pathol 46(1):62–74
Han HS, Choi KY (2021) Advances in nanomaterial-mediated photothermal cancer therapies: toward clinical applications. Biomedicines 9(3):305
Hieronymus H, Sawyers CL (2012) Traversing the genomic landscape of prostate cancer from diagnosis to death. Nat Genet 44(6):613–614
Hong G, Lee JC, Robinson JT, Raaz U, Xie L, Huang NF et al (2012) Multifunctional in vivo vascular imaging using near-infrared II fluorescence. Nat Med 18(12):1841–1846
Jain S, Thakare VS, Das M, Godugu C, Jain AK, Mathur R et al (2011) Toxicity of multiwalled carbon nanotubes with end defects critically depends on their functionalization density. Chem Res Toxicol 24(11):2028–2039

Jin CS, Overchuk M, Cui L, Wilson BC, Bristow RG, Chen J et al (2016) Nanoparticle-enabled selective destruction of prostate tumor using MRI-guided focal photothermal therapy. Prostate 76(13):1169–1181
Kafa H, Wang JT, Rubio N, Klippstein R, Costa PM, Hassan HA et al (2016) Translocation of LRP1 targeted carbon nanotubes of different diameters across the blood-brain barrier in vitro and in vivo. J Control Release 225:217–229
Kim J, Gosnell JE, Roman SA (2020) Geographic influences in the global rise of thyroid cancer. Nat Rev Endocrinol 16(1):17–29
Kumar A, White TA, MacKenzie AP, Clegg N, Lee C, Dumpit RF et al (2011) Exome sequencing identifies a spectrum of mutation frequencies in advanced and lethal prostate cancers. Proc Natl Acad Sci U S A 108(41):17087–17092
Lamartina L, Grani G, Durante C, Borget I, Filetti S, Schlumberger M (2018) Follow-up of differentiated thyroid cancer—what should (and what should not) be done. Nat Rev Endocrinol 14(9):538–551
Lee W, Jiang Z, Liu J, Haverty PM, Guan Y, Stinson J et al (2010) The mutation spectrum revealed by paired genome sequences from a lung cancer patient. Nature 465(7297):473–477
Lee SS, Roche PJ, Giannopoulos PN, Mitmaker EJ, Tamilia M, Paliouras M et al (2017) Prostate-specific membrane antigen-directed nanoparticle targeting for extreme nearfield ablation of prostate cancer cells. Tumour Biol 39(3):1010428317695943
Li Y, Liu X, Pan W, Li N, Tang B (2020) Photothermal therapy-induced immunogenic cell death based on natural melanin nanoparticles against breast cancer. Chem Commun (camb) 56(9):1389–1392
Liang X, Shang W, Chi C, Zeng C, Wang K, Fang C et al (2016) Dye-conjugated single-walled carbon nanotubes induce photothermal therapy under the guidance of near-infrared imaging. Cancer Lett 383(2):243–249
Lorite GS, Ylä-Outinen L, Janssen L, Pitkänen O, Joki T, Koivisto JT et al (2019) Carbon nanotube micropillars trigger guided growth of complex human neural stem cells networks. Nano Res 12(11):2894–2899
Lovat V, Pantarotto D, Lagostena L, Cacciari B, Grandolfo M, Righi M et al (2005) Carbon nanotube substrates boost neuronal electrical signaling. Nano Lett 5(6):1107–1110
Lu GH, Shang WT, Deng H, Han ZY, Hu M, Liang XY et al (2019) Targeting carbon nanotubes based on IGF-1R for photothermal therapy of orthotopic pancreatic cancer guided by optical imaging. Biomaterials 195:13–22
Mohammadi E, Zeinali M, Mohammadi-Sardoo M, Iranpour M, Behnam B, Mandegary A (2020) The effects of functionalization of carbon nanotubes on toxicological parameters in mice. Hum Exp Toxicol 39(9):1147–1167
Moon HK, Lee SH, Choi HC (2009) In vivo near-infrared mediated tumor destruction by photothermal effect of carbon nanotubes. ACS Nano 3(11):3707–3713
Nomura S, Morimoto Y, Tsujimoto H, Arake M, Harada M, Saitoh D et al (2020) Highly reliable, targeted photothermal cancer therapy combined with thermal dosimetry using a near-infrared absorbent. Sci Rep 10(1):9765
Panczyk T, Wolski P, Lajtar L (2016) Coadsorption of doxorubicin and selected dyes on carbon nanotubes. theoretical investigation of potential application as a ph-controlled drug delivery system. Langmuir 32(19):4719–4728
Pennes HH (1948) Analysis of tissue and arterial blood temperatures in the resting human forearm. J Appl Physiol 1(2):93–122
Pleasance ED, Cheetham RK, Stephens PJ, McBride DJ, Humphray SJ, Greenman CD et al (2010a) A comprehensive catalogue of somatic mutations from a human cancer genome. Nature 463(7278):191–196
Pleasance ED, Stephens PJ, O'Meara S, McBride DJ, Meynert A, Jones D et al (2010b) A small-cell lung cancer genome with complex signatures of tobacco exposure. Nature 463(7278):184–190
Puente XS, Pinyol M, Quesada V, Conde L, Ordonez GR, Villamor N et al (2011) Whole-genome sequencing identifies recurrent mutations in chronic lymphocytic leukaemia. Nature 475(7354):101–105
Rastinehad AR, Anastos H, Wajswol E, Winoker JS, Sfakianos JP, Doppalapudi SK et al (2019) Gold nanoshell-localized photothermal ablation of prostate tumors in a clinical pilot device study. Proc Natl Acad Sci U S A 116(37):18590–18596
Rees Smith B, McLachlan SM, Furmaniak J (1988) Autoantibodies to the thyrotropin receptor. Endocr Rev 9(1):106–121
Reitman ML (2018) Of mice and men—environmental temperature, body temperature, and treatment of obesity. FEBS Lett 592(12):2098–2107
Ren J, Xu Q, Chen X, Li W, Guo K, Zhao Y et al (2017) Superaligned carbon nanotubes guide oriented cell growth and promote electrophysiological homogeneity for synthetic cardiac tissues. Adv Mater 29(44):1702713
Robinson JT, Welsher K, Tabakman SM, Sherlock SP, Wang H, Luong R et al (2010) High performance in vivo near-IR (>1 mum) imaging and photothermal cancer therapy with carbon nanotubes. Nano Res 3(11):779–793
Sato Y, Yokoyama A, Shibata K, Akimoto Y, Ogino S, Nodasaka Y et al (2005) Influence of length on cytotoxicity of multiwalled carbon nanotubes against human acute monocytic leukemia cell line THP-1 in vitro and subcutaneous tissue of rats in vivo. Mol Biosyst 1(2):176–182
Simon J, Flahaut E, Golzio M (2019) Overview of carbon nanotubes for biomedical applications. Materials (basel) 12(4):624
Sobhani Z, Behnam MA, Emami F, Dehghanian A, Jamhiri I (2017) Photothermal therapy of melanoma tumor using multiwalled carbon nanotubes. Int J Nanomed 12:4509–4517
Sun Y, Peng Z, Li H, Wang Z, Mu Y, Zhang G et al (2019) Suspended CNT-based FET sensor for ultrasensitive and label-free detection of DNA hybridization. Biosens Bioelectron 137:255–262
Tilmaciu CM, Morris MC (2015) Carbon nanotube biosensors. Front Chem 3:59
Waltering KK, Urbanucci A, Visakorpi T (2012) Androgen receptor (AR) aberrations in castration-resistant prostate cancer. Mol Cell Endocrinol. 360(1–2):38–43
Wang TS, Sosa JA (2018) Thyroid surgery for differentiated thyroid cancer—recent advances and future directions. Nat Rev Endocrinol 14(11):670–683
Wang D, Zhang N, Jing X, Zhang Y, Xu Y, Meng L (2020) A tumor-microenvironment fully responsive nano-platform for MRI-guided photodynamic and photothermal synergistic therapy. J Mater Chem B 8(36):8271–8281
Welsher K, Sherlock SP, Dai H (2011) Deep-tissue anatomical imaging of mice using carbon nanotube fluorophores in the second near-infrared window. Proc Natl Acad Sci U S A 108(22):8943–8948
West CL, Doughty ACV, Liu K, Chen WR (2019) Monitoring tissue temperature during photothermal therapy for cancer. J BioX Res 2(4):159–168
Wilhelm S, Tavares AJ, Dai Q, Ohta S, Audet J, Dvorak HF et al (2016) Analysis of nanoparticle delivery to tumours. Nat Rev Mater 1(5):16014

Wu C, Wyatt AW, Lapuk AV, McPherson A, McConeghy BJ, Bell RH et al (2012) Integrated genome and transcriptome sequencing identifies a novel form of hybrid and aggressive prostate cancer. J Pathol 227(1):53–61
Xu X, Zhu K, Liu F, Wang Y, Shen J, Jin J et al (2013) Identification of somatic mutations in human prostate cancer by RNA-Seq. Gene 519(2)343-7
Yan H, Xue Z, Xie J, Dong Y, Ma Z, Sun X et al (2019) Toxicity of carbon nanotubes as anti-tumor drug carriers. Int J Nanomed 14:10179–10194
Yu YP, Song C, Tseng G, Ren BG, LaFramboise W, Michalopoulos G et al (2012) Genome abnormalities precede prostate cancer and predict clinical relapse. Am J Pathol 180(6):2240–2248
Zhang M, Wang W, Wu F, Yuan P, Chi C, Zhou N (2017) Magnetic and fluorescent carbon nanotubes for dual modal imaging and photothermal and chemo-therapy of cancer cells in living mice. Carbon 123:70–83
Zhang P, Yi W, Hou J, Yoo S, Jin W, Yang Q (2018) A carbon nanotube-gemcitabine-lentinan three-component composite for chemo-photothermal synergistic therapy of cancer. Int J Nanomed 13:3069–3080
Zhao Y, Zhao T, Cao Y, Sun J, Zhou Q, Chen H et al (2021) Temperature-sensitive lipid-coated carbon nanotubes for synergistic photothermal therapy and gene therapy. ACS Nano 15(4):6517–6529
Zhou F, Xing D, Ou Z, Wu B, Resasco DE, Chen WR (2009) Cancer photothermal therapy in the near-infrared region by using single-walled carbon nanotubes. J Biomed Opt 14(2):021009
Zou L, Wang H, He B, Zeng L, Tan T, Cao H et al (2016) Current approaches of photothermal therapy in treating cancer metastasis with nanotherapeutics. Theranostics 6(6):762–772

Publisher's Note

Springer Nature remains neutral with regard to jurisdictional claims in published maps and institutional affiliations.

Ready to submit your research? Choose BMC and benefit from:

- fast, convenient online submission
- thorough peer review by experienced researchers in your field
- rapid publication on acceptance
- support for research data, including large and complex data types
- gold Open Access which fosters wider collaboration and increased citations
- maximum visibility for your research: over 100M website views per year

At BMC, research is always in progress.

Learn more biomedcentral.com/submissions